CSIRO PUBLISHING

Exploration Geophysics, 2016, **47**, 158–167
http://dx.doi.org/10.1071/EG15022

Numerical dispersion analysis for three-dimensional Laplace-Fourier-domain scalar wave equation

Jing-Bo Chen

Key Laboratory of Petroleum Resources Research, Institute of Geology and Geophysics,
Chinese Academy of Sciences, PO Box 9825, Beijing 100029, China. Email: chenjb@mail.iggcas.ac.cn

Abstract. Based on the phase velocity and attenuation propagation velocity, a method for performing numerical dispersion analysis of three-dimensional Laplace-Fourier-domain scalar wave equation is presented. This method is applied to a 27-point average-derivative optimal scheme and a 27-point finite-element scheme. Within the relative error of 1%, the 27-point average-derivative optimal scheme requires seven grid points per wavelength and pseudo-wavelength while the 27-point finite-element scheme requires 23 grid points per wavelength and pseudo-wavelength for equal and unequal directional sampling intervals. Numerical examples show that the 27-point Laplace-Fourier-domain average-derivative optimal scheme is more accurate than the 27-point Laplace-Fourier-domain finite-element scheme for the same computational cost. By using larger directional sampling intervals while maintaining accuracy, the 27-point Laplace-Fourier-domain average-derivative optimal scheme can greatly reduce the computational cost of three-dimensional Laplace-Fourier-domain modelling.

Key words: 3D modelling, dispersion analysis, finite difference, Laplace-Fourier domain, optimisation.

Received 17 March 2015, accepted 4 June 2015, published online 25 June 2015

Introduction

Multiscale full waveform inversion (FWI) can extract quantitative information on the Earth's interior from a simple starting model (Bunks et al., 1995; Virieux and Operto, 2009). However, this method fails when the seismic data lack low-frequency components. To address this issue, Shin and Cha (2009) proposed the Laplace-Fourier-domain FWI which is equivalent to the complex-frequency-domain method (Brenders and Pratt, 2007). This approach can recover a long-wavelength velocity model from the seismic data lacking low-frequency information. The main idea of this method is to use the low-frequency components of the damped wavefield. For three-dimensional Laplace-Fourier-domain FWI, its computational cost is very high, and therefore it is important to develop efficient Laplace-Fourier-domain modelling schemes.

Numerical dispersion analysis for three-dimensional Laplace-Fourier-domain scalar wave equation is the foundation for developing efficient numerical modelling schemes. Um et al. (2012) performed three-dimensional Laplace-Fourier-domain dispersion analysis through numerical experiments. However, in order to construct efficient schemes based on the optimisation technique, we need to perform numerical dispersion analysis for three-dimensional Laplace-Fourier-domain scalar wave equation through the classical theory of dispersion analysis. Chen (2014*a*) developed a method for performing numerical dispersion analysis for two-dimensional Laplace-Fourier-domain scalar wave equation. This method is based on the phase velocity and attenuation propagation velocity. Using this approach, an optimal scheme is developed which requires much fewer grid points per wavelength and pseudo-wavelength in comparison with the classical scheme.

In this paper, I will generalise the method in Chen (2014*a*) and develop a method for performing numerical dispersion analysis for three-dimensional Laplace-Fourier-domain scalar wave equation. Due to the presence of the azimuth angle, the three-dimensional version of the two-dimensional Laplace-Fourier-domain dispersion analysis method becomes complicated. Two 27-point schemes will be considered: one is the optimal average-derivative scheme; the other is the finite-element scheme. I choose the 27-point scheme for two reasons: 1) it has more degrees of freedom, which is appropriate for Laplace-Fourier-domain modelling; 2) I can make fair comparisons with a currently used 27-point finite-element scheme.

First, I will present the two 27-point schemes and discuss their relationship. This is followed by the optimisation of coefficients and a numerical dispersion analysis. Numerical comparisons with the analytical solution are then presented to demonstrate the theoretical analysis.

Theory and methods

The 3D Laplace-Fourier-domain scalar wave equation can be written as

$$\frac{\partial^2 P}{\partial x^2}+\frac{\partial^2 P}{\partial y^2}+\frac{\partial^2 P}{\partial z^2}+\frac{(\omega+\mathrm{i}s)^2}{v^2}P=0, \qquad (1)$$

where P is the pressure wavefield; x, y, and z are coordinates of the media, ω is the angular frequency; s is the Laplace damping constant; $\mathrm{i}=\sqrt{-1}$; and $v(x, y, z)$ is the velocity.

A 27-point average-derivative scheme for Equation 1 can be obtained as follows (see Figure 1*a*):

$$\frac{\bar{P}_{m+1,l,n}-2\bar{P}_{m,l,n}+\bar{P}_{m-1,l,n}}{\Delta x^2}+\frac{\hat{P}_{m,l+1,n}-2\hat{P}_{m,l,n}+\hat{P}_{m,l-1,n}}{\Delta y^2}+\frac{\tilde{P}_{m,l,n+1}-2\tilde{P}_{m,l,n}+\tilde{P}_{m,l,n-1}}{\Delta z^2}+\frac{(\omega+\mathrm{i}s)^2}{v_{m,l,n}^2}\left(cP_{m,l,n}+dA+eB+fC\right)=0, \tag{2}$$

where

$$\bar{P}_{m+j,l,n}=\alpha_1\left(P_{m+j,l+1,n}+P_{m+j,l,n+1}+P_{m+j,l-1,n}+P_{m+j,l,n-1}\right)+\alpha_2\left(P_{m+j,l+1,n+1}+P_{m+j,l-1,n+1}+P_{m+j,l+1,n-1}+P_{m+j,l-1,n-1}\right)+(1-4\alpha_1-4\alpha_2)P_{m+j,l,n},\ j=1,0,-1,$$

$$\hat{P}_{m,l+j,n}=\beta_1\left(P_{m+1,l+j,n}+P_{m,l+j,n+1}+P_{m-1,l+j,n}+P_{m,l+j,n-1}\right)+\beta_2\left(P_{m+1,l+j,n+1}+P_{m+1,l+j,n-1}+P_{m-1,l+j,n+1}+P_{m-1,l+j,n-1}\right)+(1-4\beta_1-4\beta_2)P_{m,l+j,n},\ j=1,0,-1,$$

$$\tilde{P}_{m,l,n+j}=\gamma_1\left(P_{m+1,l,n+j}+P_{m,l+1,n+j}+P_{m-1,l,n+j}+P_{m,l-1,n+j}\right)+\gamma_2\left(P_{m+1,l+1,n+j}+P_{m+1,l-1,n+j}+P_{m-1,l+1,n+j}+P_{m-1,l-1,n+j}\right)+(1-4\gamma_1-4\gamma_2)P_{m,l,n+j},\ j=1,0-1,$$

$$A=\left(P_{m,l+1,n}+P_{m,l,n+1}+P_{m,l-1,n}+P_{m,l,n-1}+P_{m+1,l,n}+P_{m-1,l,n}\right),$$

$$B=\left(P_{m+1,l+1,n}+P_{m+1,l,n+1}+P_{m+1,l-1,n}+P_{m+1,l,n-1}+P_{m-1,l+1,n}+P_{m-1,l,n+1}+P_{m-1,l-1,n}+P_{m-1,l,n-1}+P_{m,l+1,n+1}+P_{m,l-1,n+1}+P_{m,l+1,n-1}+P_{m,l-1,n-1}\right),$$

$$C=\left(P_{m+1,l+1,n+1}+P_{m+1,l-1,n+1}+P_{m+1,l+1,n-1}+P_{m+1,l,n-1}+P_{m-1,l+1,n+1}+P_{m-1,l-1,n+1}+P_{m-1,l+1,n-1}+P_{m-1,l-1,n-1}\right),$$

where $P_{m,l,n}\approx P(m\Delta x, l\Delta y, n\Delta z)$; $v_{m,l,n}\approx v(m\Delta x, l\Delta y, n\Delta z)$; m, l, and n are integer indices in the x, y, and z directions; Δx, Δy, and Δz are directional sampling intervals; α_1, α_2, β_1, β_2, γ_1, γ_2, c, d, and e are coefficients that can be optimised; and $f=\frac{1-c-6d-12e}{8}$.

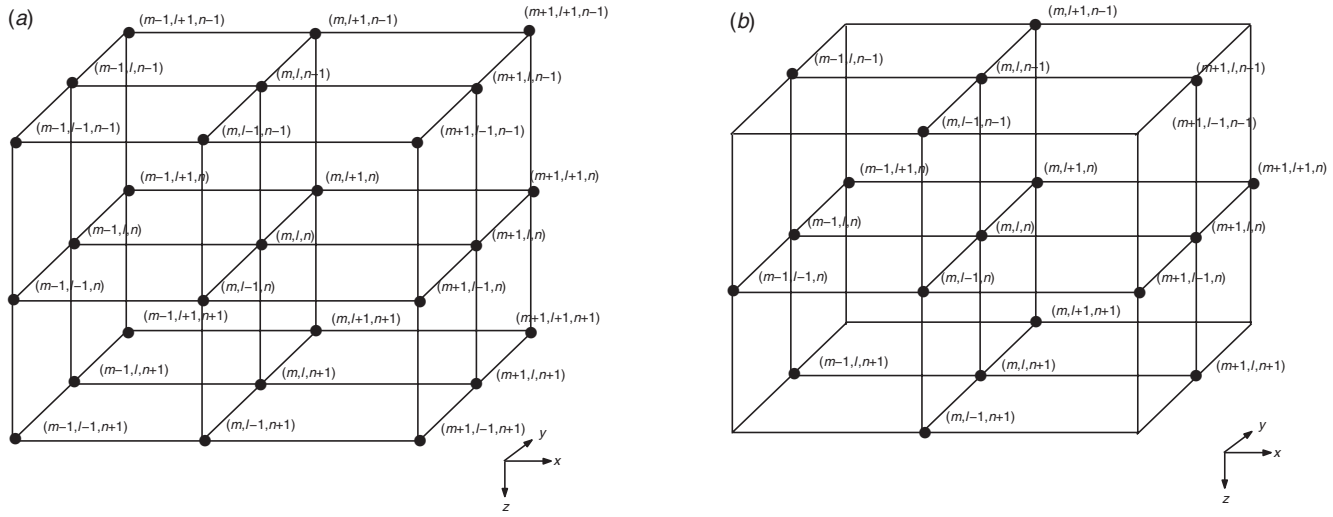

Fig. 1. Stencils of the (*a*) 27-point and (*b*) 19-point average-derivative optimal schemes for 3D Laplace-Fourier-domain scalar wave equation.

Table 1. Laplace-Fourier-domain optimisation coefficients for α_1, α_2, β_1, β_2, γ_1, γ_2, c, d and e for different $r_1=\frac{\Delta x}{\Delta y}$ and $r_2=\frac{\Delta x}{\Delta z}$ when $\Delta x=\max\{\Delta x, \Delta y, \Delta z\}$.

	α_1	α_2	β_1	β_2	γ_1	γ_2	c	d	e
$r_1=1$ $r_2=1$	0.083357	0.000000	0.083358	0.000000	0.083359	0.000000	0.499969	0.083338	0.000000
$r_1=1$ $r_2=2$	0.083375	0.000000	0.083357	0.000000	0.083358	0.000000	0.499935	0.083344	0.000000
$r_1=1$ $r_2=3$	0.061282	0.011042	0.077572	0.002895	0.080267	0.001542	0.499944	0.083342	0.000000
$r_1=2$ $r_2=1$	0.080729	0.001306	0.081738	0.000803	0.080351	0.001506	0.499972	0.083337	0.000000
$r_1=2$ $r_2=2$	0.037452	0.022981	0.074811	0.004263	0.072099	0.005619	0.499961	0.083339	0.000000
$r_1=2$ $r_2=3$	0.030901	0.026307	0.028492	0.027398	0.056631	0.013347	0.499994	0.083334	0.000000
$r_1=3$ $r_2=1$	0.062409	0.010434	0.072944	0.005197	0.070313	0.006548	0.499993	0.083334	0.000000
$r_1=3$ $r_2=2$	0.018739	0.032358	0.056363	0.013484	0.035135	0.024090	0.499987	0.083335	0.000000
$r_1=3$ $r_2=3$	0.002120	0.040691	0.000401	0.041458	0.000904	0.0412208	0.500005	0.083332	0.000000

Equation 2 is the Laplace-Fourier-domain version of a 27-point frequency-domain scheme (Chen 2014*b*).

Although a computational scheme is not handled explicitly in the finite-element method, a numerical scheme can be extracted from the assembled matrix (Pyun et al., 2011). Pyun et al. (2011) presented a 27-point finite-element scheme:

$$\frac{\mathcal{D}_{xx}}{36\Delta x^2}+\frac{\mathcal{D}_{yy}}{36\Delta y^2}+\frac{\mathcal{D}_{zz}}{36\Delta z^2}+\frac{(\omega+\mathrm{i}s)^2}{v_{m,l,n}^2}P_{m,l,n}=0, \qquad (3)$$

where

$$\begin{aligned}\mathcal{D}_{xx}=&P_{m+1,l-1,n-1}-2P_{m,l-1,n-1}+P_{m-1,l-1,n-1}\\&+4P_{m+1,l-1,n}-8P_{m,l-1,n}+4P_{m-1,l-1,n}+P_{m+1,l-1,n+1}\\&-2P_{m,l-1,n+1}+2P_{m-1,l-1,n+1}+4P_{m+1,l,n-1}-8P_{m,l,n-1}\\&+4P_{m-1,l,n-1}+16P_{m+1,l,n}-32P_{m,l,n}+16P_{m-1,l,n}\\&+4P_{m+1,l,n+1}-8P_{m,l,n+1}+4P_{m-1,l,n+1}+P_{m+1,l+1,n-1}\\&-2P_{m,l+1,n-1}+P_{m-1,l+1,n-1}+4P_{m+1,l+1,n}-8P_{m,l+1,n}\\&+4P_{m-1,l+1,n}+P_{m+1,l+1,n+1}-2P_{m,l+1,n+1}+P_{m-1,l+1,n+1},\end{aligned}$$

$$\begin{aligned}\mathcal{D}_{yy}=&P_{m-1,l+1,n-1}-2P_{m-1,l,n-1}+P_{m-1,l-1,n-1}\\&+4P_{m-1,l+1,n}-8P_{m-1,l,n}+4P_{m-1,l-1,n}+P_{m-1,l+1,n+1}\\&-2P_{m-1,l,n+1}+2P_{m-1,l-1,n+1}+4P_{m,l+1,n-1}-8P_{m,l,n-1}\\&+4P_{m,l-1,n-1}+16P_{m,l+1,n}-32P_{m,l,n}+16P_{m,l-1,n}\\&+4P_{m,l+1,n+1}-8P_{m,l,n+1}+4P_{m,l-1,n+1}+P_{m+1,l+1,n-1}\\&-2P_{m+1,l,n-1}+P_{m+1,l-1,n-1}+4P_{m+1,l+1,n}-8P_{m+1,l,n}\\&+4P_{m+1,l-1,n}+P_{m+1,l+1,n+1}-2P_{m+1,l,n+1}+P_{m+1,l-1,n+1},\end{aligned}$$

$$\begin{aligned}\mathcal{D}_{zz}=&P_{m-1,l-1,n+1}-2P_{m-1,l-1,n}+P_{m-1,l-1,n-1}\\&+4P_{m-1,l,n+1}-8P_{m-1,l,n}+4P_{m-1,l,n-1}+P_{m-1,l+1,n+1}\\&-2P_{m-1,l+1,n}+2P_{m-1,l+1,n-1}+4P_{m,l-1,n+1}-8P_{m,l-1,n}\\&+4P_{m,l-1,n-1}+16P_{m,l,n+1}-32P_{m,l,n}+16P_{m,l,n-1}\\&+4P_{m,l+1,n+1}-8P_{m,l+1,n}+4P_{m,l+1,n-1}+P_{m+1,l-1,n+1}\\&-2P_{m+1,l-1,n}+P_{m+1,l-1,n-1}+4P_{m+1,l,n+1}-8P_{m+1,l,n}\\&+4P_{m+1,l,n-1}+P_{m+1,l+1,n+1}-2P_{m+1,l+1,n}+P_{m+1,l+1,n-1}.\end{aligned}$$

We can see that when $\alpha_1=\beta_1=\gamma_1=\frac{1}{9}$, $\alpha_2=\beta_2=\gamma_2=\frac{1}{36}$, $c=1$, and $d=e=0$, Equation 2 becomes Equation 3. Therefore,

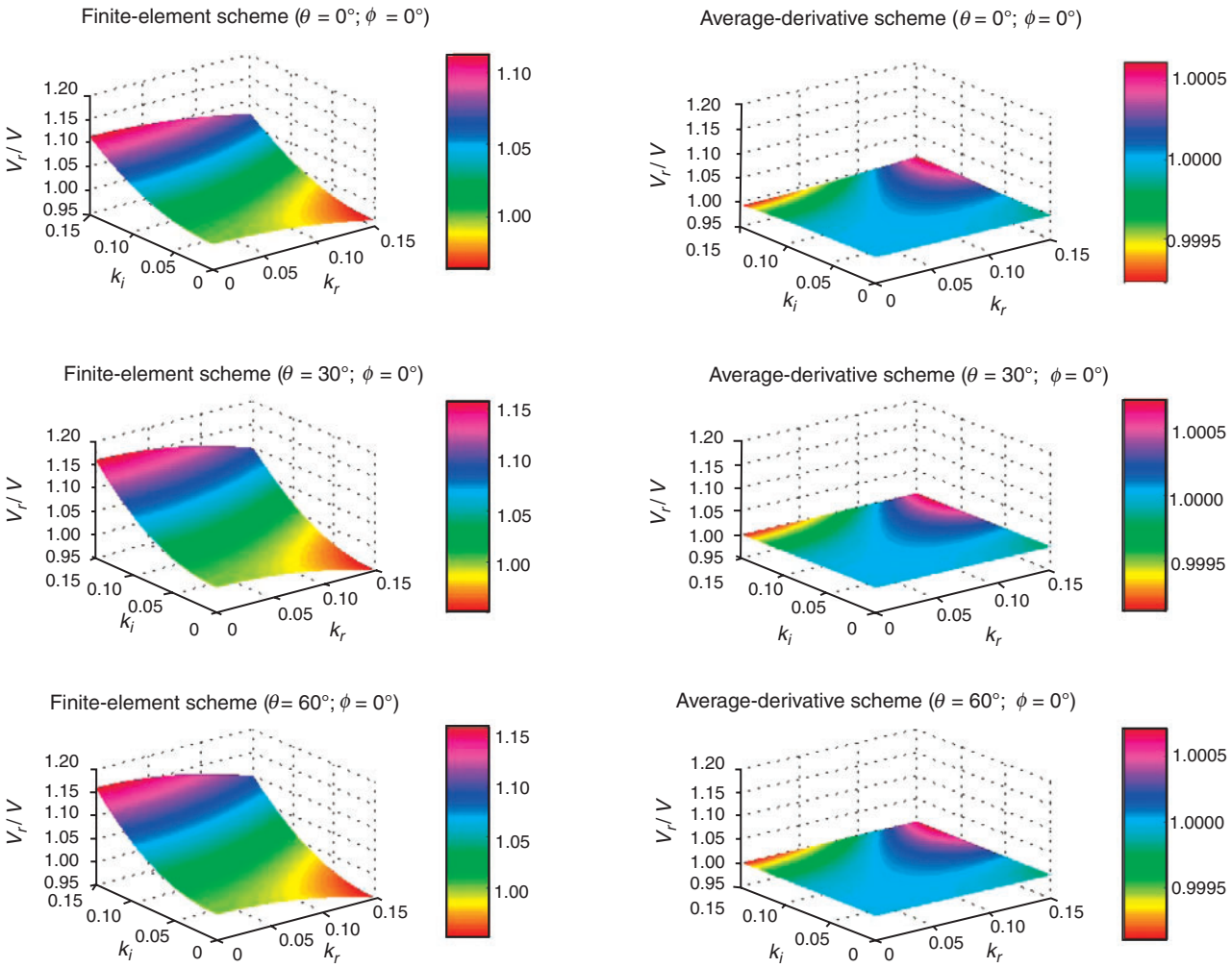

Fig. 2. Normalised phase velocity of the 27-point finite-element scheme and the 27-point average-derivative optimal scheme for fixed azimuth angle ϕ and different propagation angles θ when $r_1=1$ and $r_2=1$. The average-derivative scheme is much more accurate than the finite-element scheme for this case.

the 27-point average-derivative optimal scheme (Equation 2) includes the 27-point finite-element scheme (Equation 3) as a special case.

Consider an attenuating plane wave in the following form

$$P(k,x,y,z) = P_0 e^{ik(\sin\theta\cos\phi\, x + \sin\theta\sin\phi\, y + \cos\theta\, z)}, \tag{4}$$

where P_0 is the amplitude at $x=y=z=0$, θ is the propagation angle, ϕ is the azimuth angle, and $k = k_r + i\, k_i$. Here $k_r = \frac{\omega}{v}$ is the wavenumber, and $k_i = \frac{s}{v}$ is the pseudo-wavenumber (Chen 2014*a*).

Substituting Equation 4 into Equation 2 and assuming a constant v, we obtain the discrete dispersion relation

$$\frac{(\omega + \mathrm{i}\, s)^2}{v^2} = \frac{\mathcal{A}}{\mathcal{B}\Delta x^2}, \tag{5}$$

where

$$\begin{aligned}\mathcal{A} &= 2[1-\cos(k\sin\theta\cos\phi\,\Delta x)]E_x + 2r_1^2 \\ &\quad [1-\cos(k\sin\theta\sin\phi\,\Delta x/r_1)-1]E_y \\ &\quad + 2r_2^2[\cos(k\cos\theta\,\Delta x/r_2)-1]E_z, \\ \mathcal{B} &= c + 2d\tilde{A} + 4e\tilde{B} + 8f\tilde{C},\end{aligned}$$

where $r_1 = \frac{\Delta x}{\Delta y}$, $r_2 = \frac{\Delta x}{\Delta z}$, and

$$\begin{aligned}E_x &= 2\alpha_1(\cos(k\sin\theta\sin\phi\,\Delta x/r_1) + \cos(k\cos\theta\,\Delta x/r_2)) \\ &\quad + 4\alpha_2\cos(k\sin\theta\sin\phi\,\Delta x/r_1)\cos(k\cos\theta\,\Delta x/r_2) \\ &\quad + (1-4\alpha_1-4\alpha_2), \\ E_y &= 2\beta_1(\cos(k\sin\theta\cos\phi\,\Delta x) + \cos(k\cos\theta\,\Delta x/r_2)) \\ &\quad + 4\beta_2\cos(k\sin\theta\cos\phi\,\Delta x)\cos(k\cos\theta\,\Delta x/r_2) \\ &\quad + (1-4\beta_1-4\beta_2), \\ E_z &= 2\gamma_1(\cos(\sin\theta\cos\phi\,\Delta x) + \cos(k\sin\theta\sin\phi\,\Delta x/r_1)) \\ &\quad + 4\gamma_2\cos(k\sin\theta\cos\phi\,\Delta x)\cos(k\sin\theta\sin\phi\,\Delta x/r_1) \\ &\quad + (1-4\gamma_1-4\gamma_2), \\ \tilde{A} &= \cos(k\sin\theta\cos\phi\,\Delta x) + \cos(k\sin\theta\sin\phi\,\Delta x/r_1) \\ &\quad + \cos(k\cos\theta\,\Delta x/r_2), \\ \tilde{B} &= \cos(k\sin\theta\cos\phi\,\Delta x)\cos(k\sin\theta\sin\phi\,\Delta x/r_1) \\ &\quad + \cos(k\sin\theta\cos\phi\,\Delta x)\cos(k\cos\theta\,\Delta x/r_2) \\ &\quad + \cos(k\sin\theta\sin\phi\,\Delta x/r_1)\cos(k\cos\theta\,\Delta x/r_2), \\ \tilde{C} &= \cos(k\sin\theta\cos\phi\,\Delta x)\cos(k\sin\theta\sin\phi\,\Delta x/r_1) \\ &\quad \cos(k\cos\theta\,\Delta x/r_2).\end{aligned}$$

We can express $k\Delta x$ as

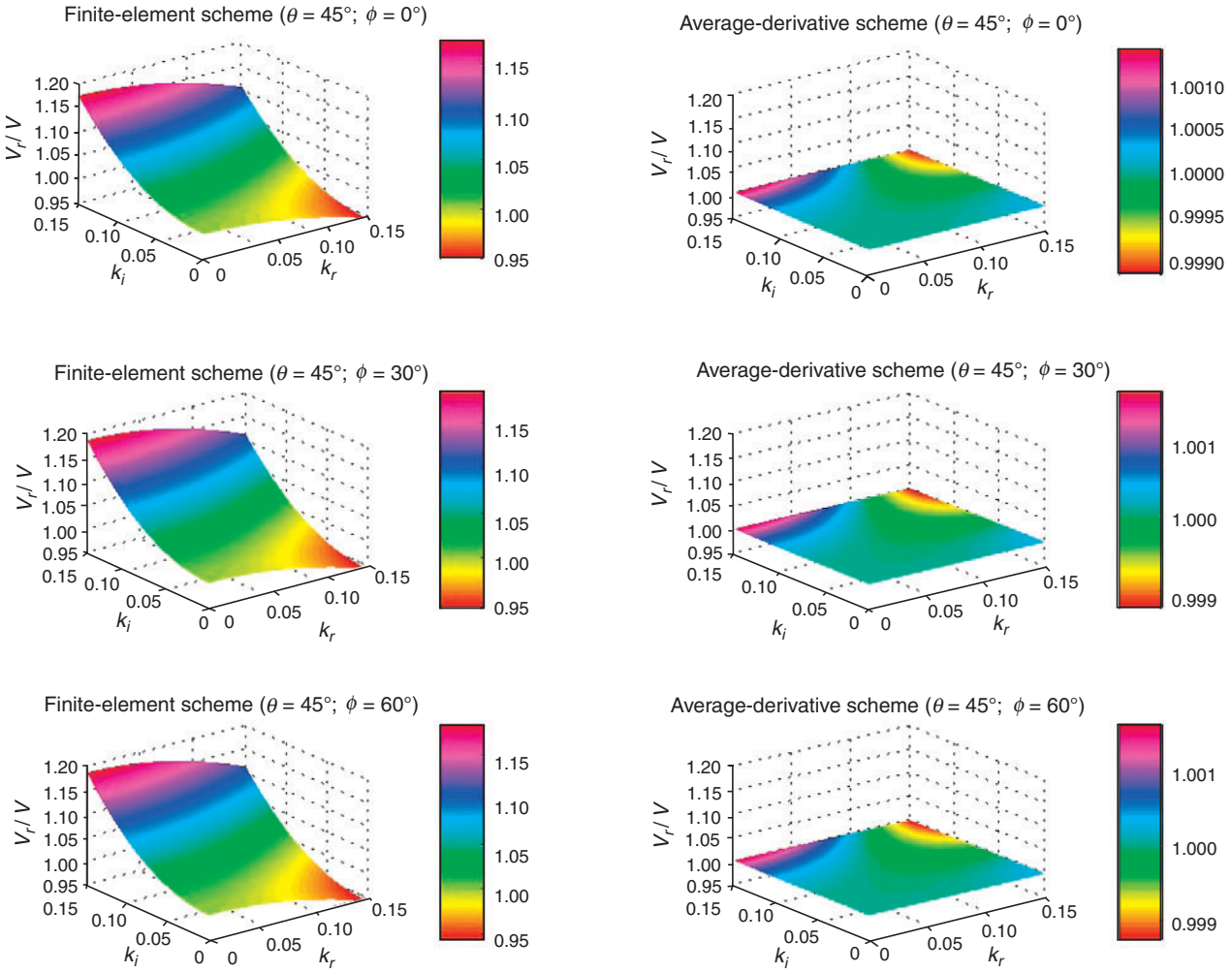

Fig. 3. Normalised phase velocity surfaces of the 27-point finite-element scheme and the 27-point average-derivative optimal scheme for fixed propagation angle θ and different azimuth angles ϕ when $r_1 = 1$ and $r_2 = 1$. The average-derivative scheme is much more accurate than the finite-element scheme for this case.

$$k\Delta x = k_r\Delta x + \mathrm{i}\, k_i\Delta x = \frac{2\pi}{G_r} + \mathrm{i}\,\frac{2\pi}{G_i}, \tag{6}$$

where $G_r = \frac{2\pi}{k_r\Delta x}$ is the number of grid points per wavelength, and $G_i = \frac{2\pi}{k_i\Delta x}$ is the number of grid points per pseudo-wavelength. Here, I assume that $\Delta x = \max\{\Delta x, \Delta y, \Delta z\}$. For other cases, similar analyses can be performed. If $\Delta y = \max\{\Delta x, \Delta y, \Delta z\}$, r_1, r_2, G_r, and G_i should be defined as $r_1 = \frac{\Delta y}{\Delta x}$, $r_2 = \frac{\Delta y}{\Delta z}$, $G_r = \frac{2\pi}{k_r\Delta y}$, and $G_i = \frac{2\pi}{k_i\Delta y}$, respectively. If $\Delta z = \max\{\Delta x, \Delta y, \Delta z\}$, r_1, r_2, G_r, and G_i should be defined as $r_1 = \frac{\Delta z}{\Delta x}$ and $r_2 = \frac{\Delta z}{\Delta y}$, $G_r = \frac{2\pi}{k_r\Delta z}$, and $G_i = \frac{2\pi}{k_i\Delta z}$, respectively.

Set

$$\sqrt{\frac{\mathcal{A}}{\mathcal{B}}} = \mathcal{F}_r(G_r, G_i, \theta, \phi) + \mathrm{i}\mathcal{F}_i(G_r, G_i, \theta, \phi). \tag{7}$$

where $\mathcal{F}_r(G_r, G_i, \theta, \phi)$ and $\mathcal{F}_i(G_r, G_i, \theta, \phi)$ are the real and imaginary parts of $\sqrt{\frac{\mathcal{A}}{\mathcal{B}}}$, respectively.

From Equations 5 and 7, we can obtain

$$\frac{\omega}{v} = \frac{1}{\Delta x}\mathcal{F}_r(G_r, G_i, \theta, \phi), \tag{8}$$

$$\frac{s}{v} = \frac{1}{\Delta x}\mathcal{F}_i(G_r, G_i, \theta, \phi). \tag{9}$$

From Equations 8 and 9, normalised numerical phase velocity and numerical attenuation propagation velocity can be obtained as follows:

$$\frac{v_r}{v} = \frac{G_r}{2\pi}\mathcal{F}_r(G_r, G_i, \theta, \phi), \tag{10}$$

$$\frac{v_i}{v} = \frac{G_i}{2\pi}\mathcal{F}_i(G_r, G_i, \theta, \phi), \tag{11}$$

where $v_r = \frac{\omega}{k_r}$ and $v_i = \frac{s}{k_i}$.

The coefficients $\alpha_1, \alpha_2, \beta_1, \beta_2, \gamma_1, \gamma_2, c, d$, and e are determined by minimising the velocity error:

$$E(\alpha_1, \alpha_2, \beta_1, \beta_2, \gamma_1, \gamma_2, c, d, e) = \int\int\int\int \left[\left(1 - \frac{v_r(\tilde{k}_r, \tilde{k}_i, \theta, \phi; \alpha_1, \alpha_2, \beta_1, \beta_2, \gamma_1, \gamma_2, c, d, e)}{v}\right)^2 + \left(1 - \frac{v_i(\tilde{k}_r, \tilde{k}_i, \theta, \phi; \alpha_1, \alpha_2, \beta_1, \beta_2, \gamma_1, \gamma_2, c, d, e)}{v}\right)^2\right] d\tilde{k}_r\, d\tilde{k}_i\, d\theta\, d\phi, \tag{12}$$

where $\tilde{k}_r = \frac{1}{G_r}$ and $\tilde{k}_i = \frac{1}{G_i}$.

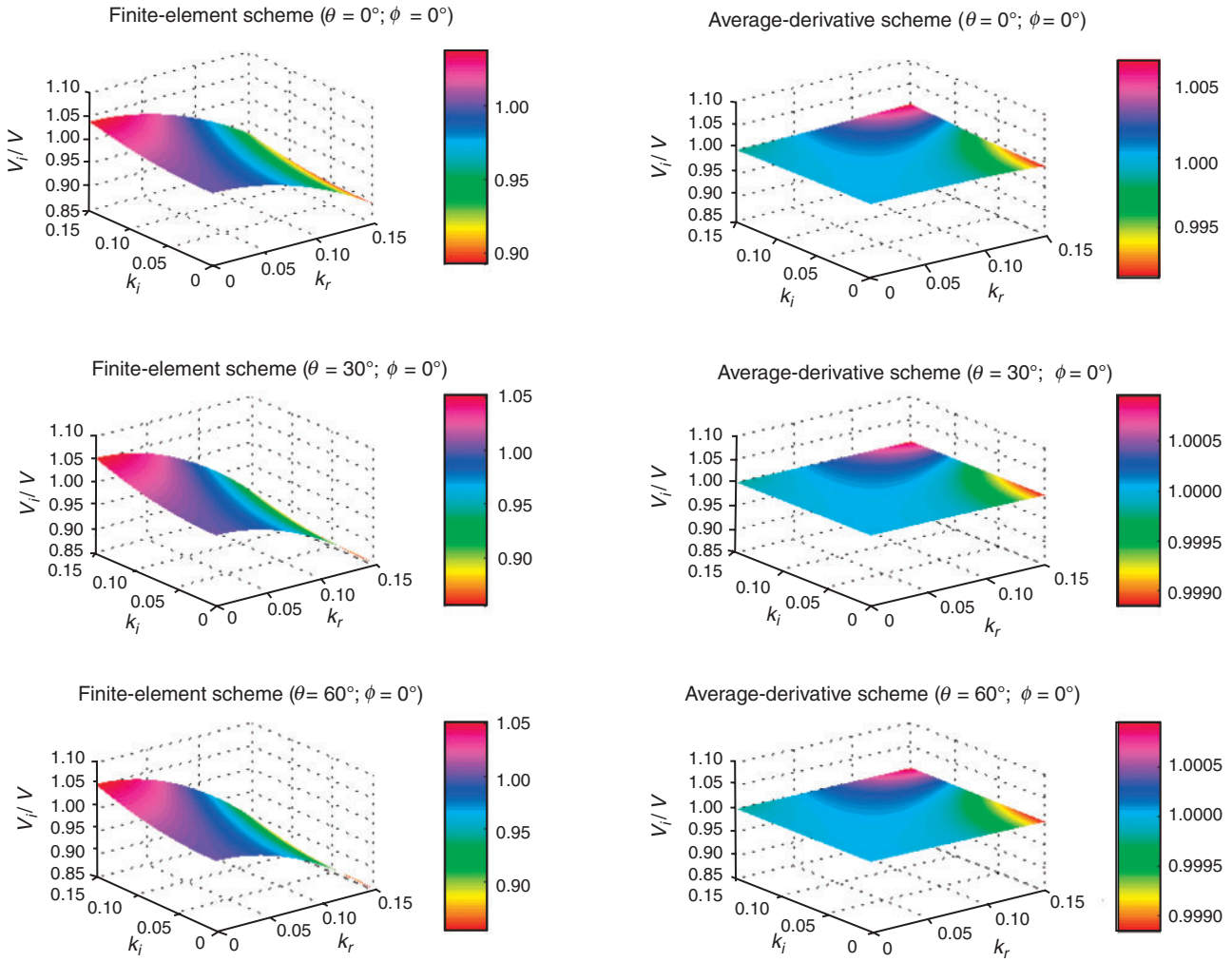

Fig. 4. Normalised attenuation propagation velocity surfaces of the 27-point finite-element scheme and the 27-point average-derivative optimal scheme for fixed azimuth angle ϕ and different propagation angles θ when $r_1 = 1$ and $r_2 = 1$. The average-derivative scheme is much more accurate than the finite-element scheme for this case.

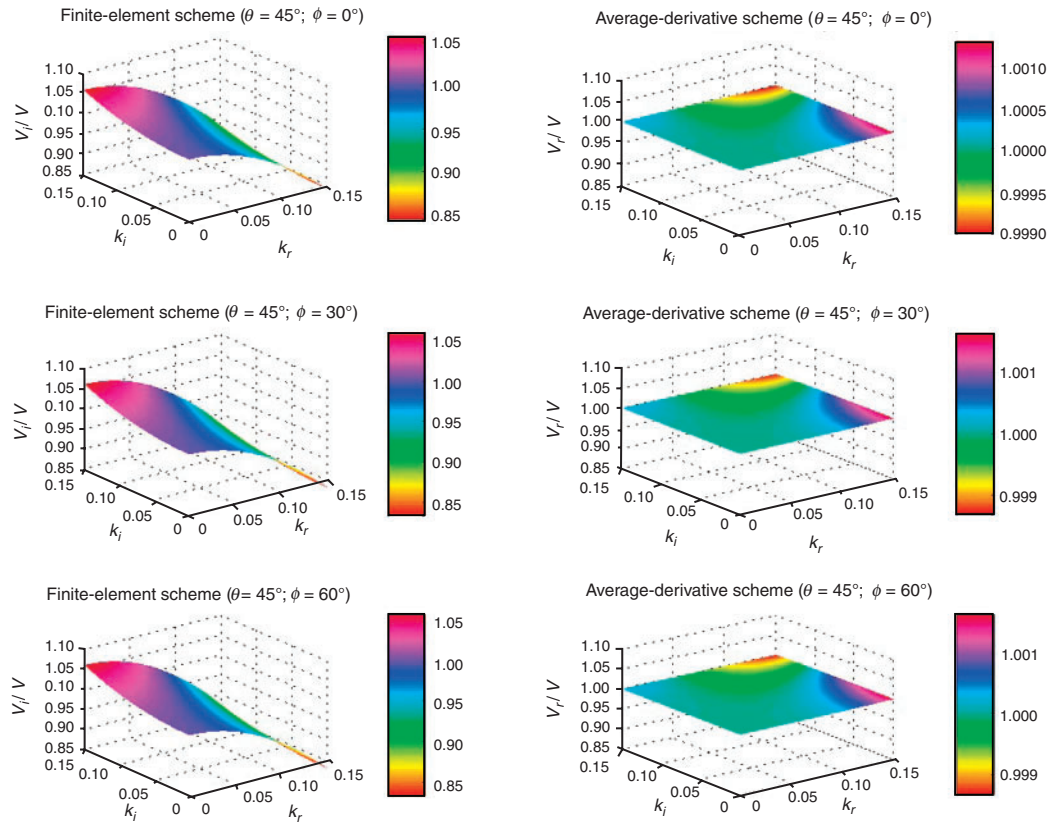

Fig. 5. Normalised attenuation propagation velocity surfaces of the 27-point finite-element scheme and the 27-point average-derivative optimal scheme for fixed propagation angle θ and different azimuth angles ϕ when $r_1 = 1$ and $r_2 = 1$. The average-derivative scheme is much more accurate than the finite-element scheme for this case.

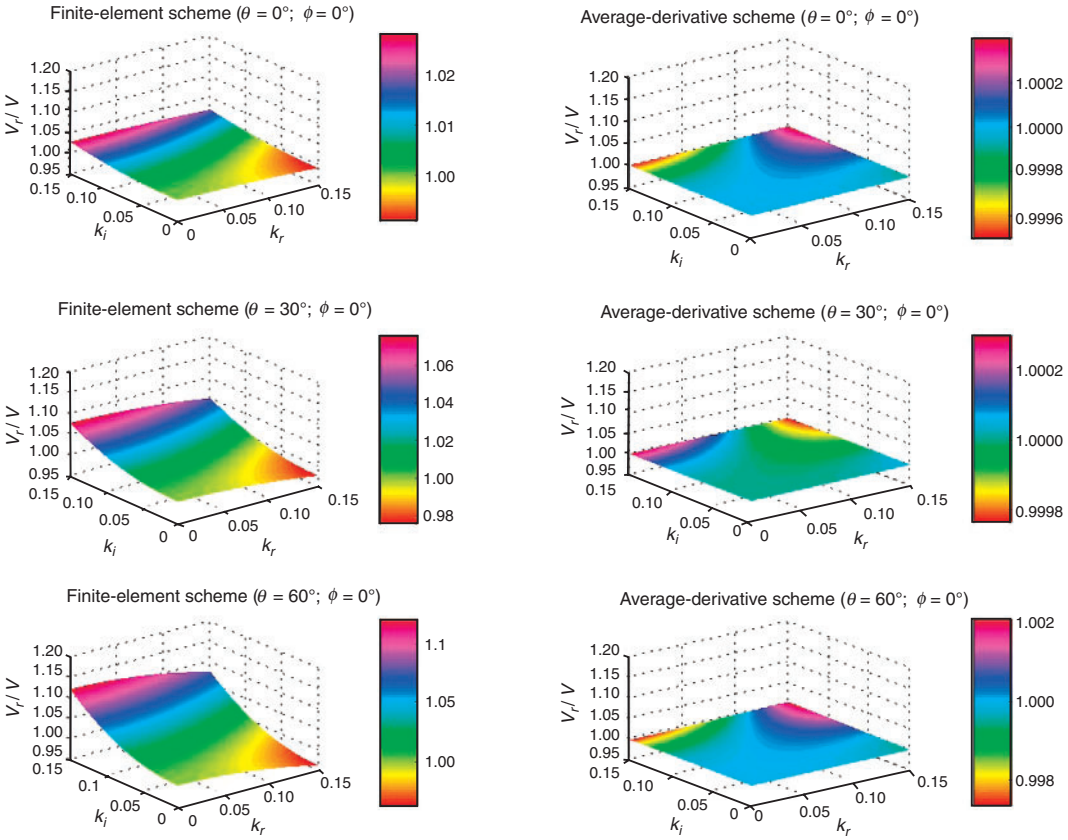

Fig. 6. Normalised phase propagation velocity surfaces of the 27-point finite-element scheme and the 27-point average-derivative optimal scheme for fixed azimuth angle ϕ and different propagation angles θ when $r_1 = 1$ and $r_2 = 2$. The average-derivative scheme is much more accurate than the finite-element scheme for this case.

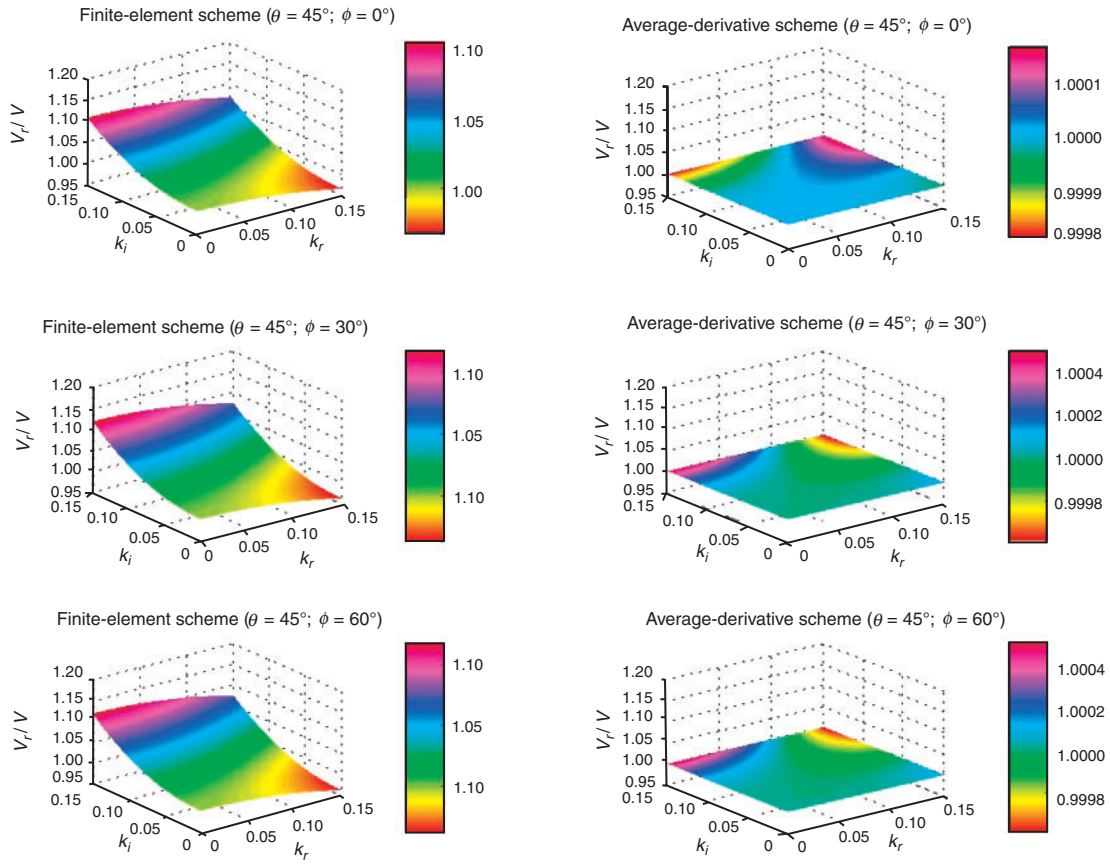

Fig. 7. Normalised phase velocity surfaces of the 27-point finite-element scheme and the 27-point average-derivative optimal scheme for fixed propagation angle θ and different azimuth angles ϕ when $r_1 = 1$ and $r_2 = 2$. The average-derivative scheme is much more accurate than the finite-element scheme for this case.

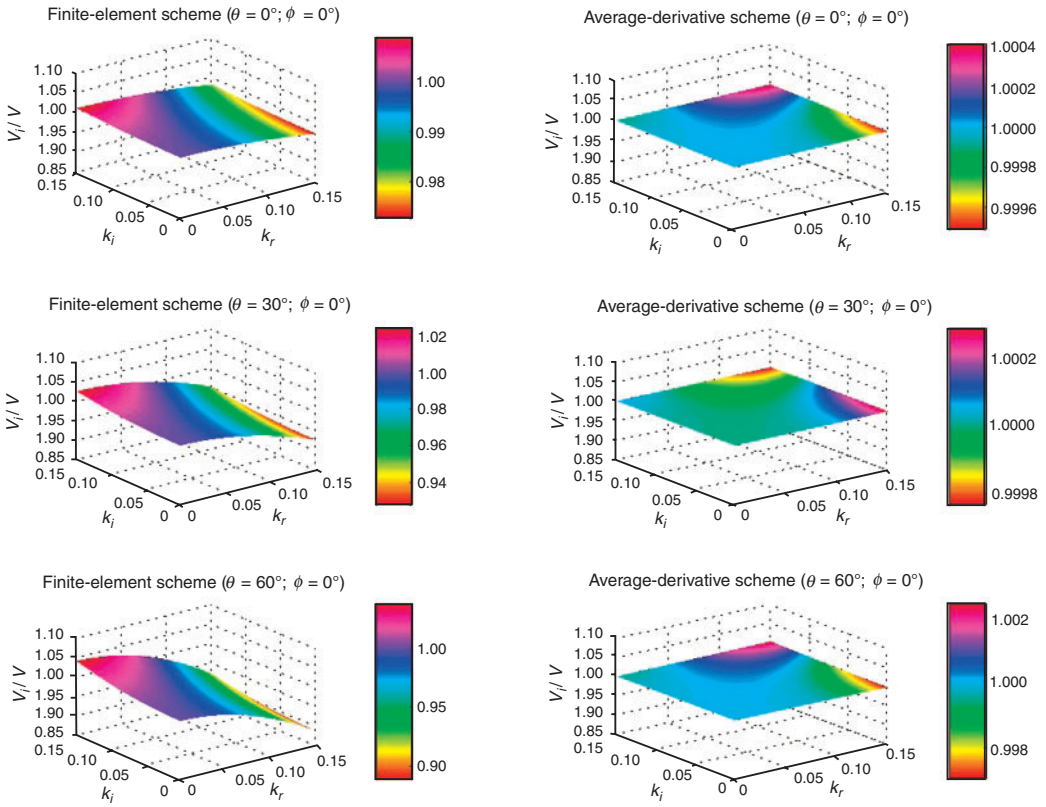

Fig. 8. Normalised attenuation propagation velocity surfaces of the 27-point finite-element scheme and the 27-point average-derivative optimal scheme for fixed azimuth angle ϕ and different propagation angles θ when $r_1 = 1$ and $r_2 = 2$. The average-derivative scheme is much more accurate than the finite-element scheme for this case.

The ranges of $\tilde{k}_r$, $\tilde{k}_i$, θ, and ϕ are taken as [0, 0.15], [0, 0.15], $[0, \frac{\pi}{2}]$, and $[0, \frac{\pi}{2}]$, respectively. The optimisation coefficients for different $r_1 = \frac{\Delta x}{\Delta y}$ and $r_2 = \frac{\Delta x}{\Delta z}$ when $\Delta x = \max\{\Delta x, \Delta y, \Delta z\}$ are listed in Table 1. We can see that the coefficients $\alpha_1, \alpha_2, \beta_1, \beta_2, \gamma_1$, and γ_2 vary with r_1 and r_2, and the changes in coefficients c, d, and e are small. For the two cases where $r_1 = 1$, $r_2 = 1$ and $r_1 = 1$, $r_2 = 2$, we can see that $\alpha_2 = \beta_2 = \gamma_2 = 0$ and $f = \frac{1-c-6d-12e}{8} = 0$. Therefore, in these two cases, the 27-point scheme (Equation 2) reduces to a 19-point scheme (see Figure 1*b*). For convenience, however, Equation 2 will still be called a 27-point scheme in these two cases with the coefficients for the eight corner points being zero.

Results

Dispersion analysis

I performed numerical dispersion analysis by using Equations 10 and 11. First, I considered the case where $r_1 = 1$ and $r_2 = 1$, which corresponds to the equal directional intervals $\Delta x = \Delta y = \Delta z$. Figure 2 shows normalised phase velocity surfaces of the 27-point finite-element scheme and the 27-point average-derivative optimal scheme for fixed azimuth angle ϕ and different propagation angles θ when $r_1 = 1$ and $r_2 = 1$. For the 27-point finite-element scheme, the errors increase from $\theta = 0^o$ to $\theta = 30^o$. This is probably because the finite-element scheme inherits the dispersion features of un-optimised schemes. Due to the complementary property of the trigonometrical functions, the errors for $\theta = 30^o$ and $\theta = 60^o$ are the same. For the 27-point average-derivative optimal scheme, the errors are within 1%. Figure 3 shows normalised phase velocity surfaces of the 27-point finite-element scheme and the 27-point average-derivative optimal scheme for fixed propagation angle θ and different azimuth angles ϕ when $r_1 = 1$ and $r_2 = 1$. In this case, both schemes show symmetry with respect to the azimuth angle. However, the 27-point finite-element scheme exhibits large errors because it is an un-optimised scheme.

Figure 4 displays normalised attenuation propagation velocity surfaces of the 27-point finite-element scheme and the 27-point average-derivative optimal scheme for fixed azimuth angle ϕ and different propagation angles θ when $r_1 = 1$ and $r_2 = 1$. We can see that the surfaces in Figures 4 and 5 have quite different shapes from those in Figures 2 and 3. However, with respect to the errors, the same conclusion can be drawn.

Figures 6–9 show the surfaces for the case where $r_1 = 1$ and $r_2 = 2$. For both the 27-point finite-element scheme and the 27-point average-derivative optimal scheme, the errors are slightly smaller than that in the case where $r_1 = 1$ and $r_2 = 1$ due to smaller Δz.

From Figures 2–9, we can conclude that within the relative error of 1%, the 27-point finite-element scheme (Equation 3) requires 23 grid points per wavelength and pseudo-wavelength, while the 27-point average-derivative optimal scheme (Equation 2) requires seven grid points per wavelength and pseudo-wavelength for both equal and unequal directional sampling intervals.

Numerical experiments

Numerical experiments were performed to verify the theoretical analysis on the 27-point finite-element scheme (Equation 3) and the 27-point average-derivative optimal scheme (Equation 2). I considered a homogeneous velocity model with a velocity of 3500 m/s (Figure 10*a*). Horizontal and vertical distances are

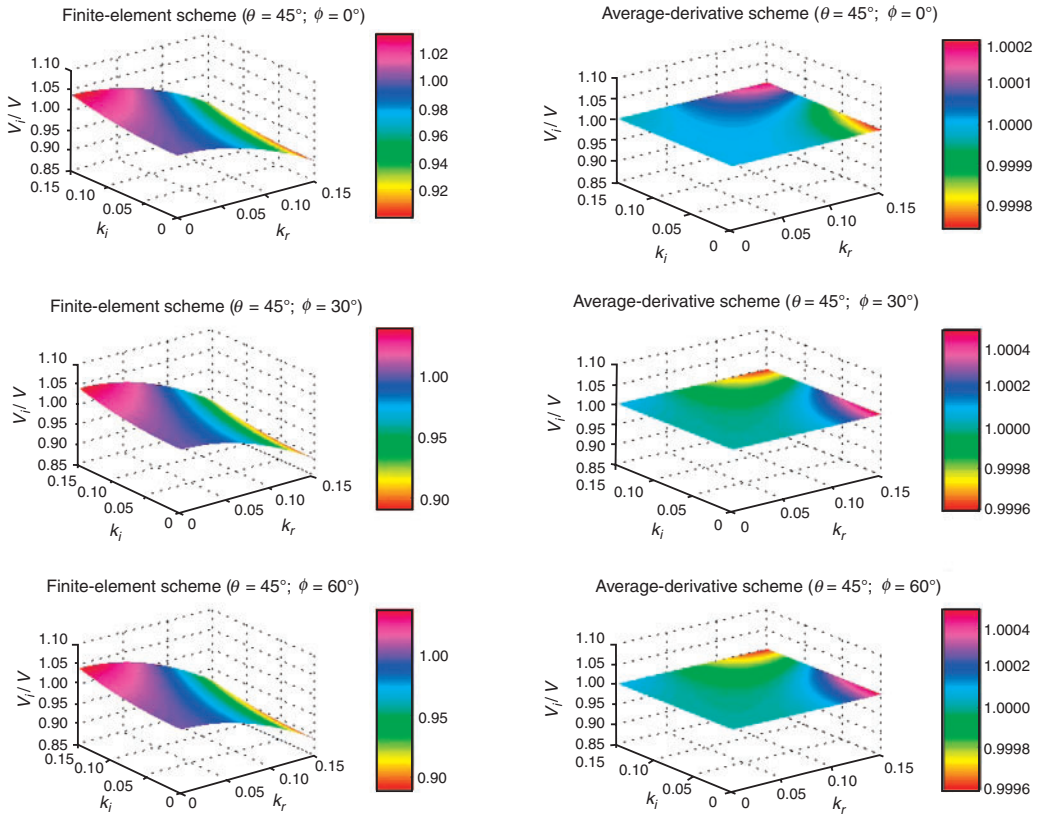

Fig. 9. Normalised attenuation propagation velocity surfaces of the 27-point finite-element scheme and the 27-point average-derivative optimal scheme for fixed propagation angle θ and different azimuth angles ϕ when $r_1 = 1$ and $r_2 = 2$. The average-derivative scheme is much more accurate than the finite-element scheme for this case.

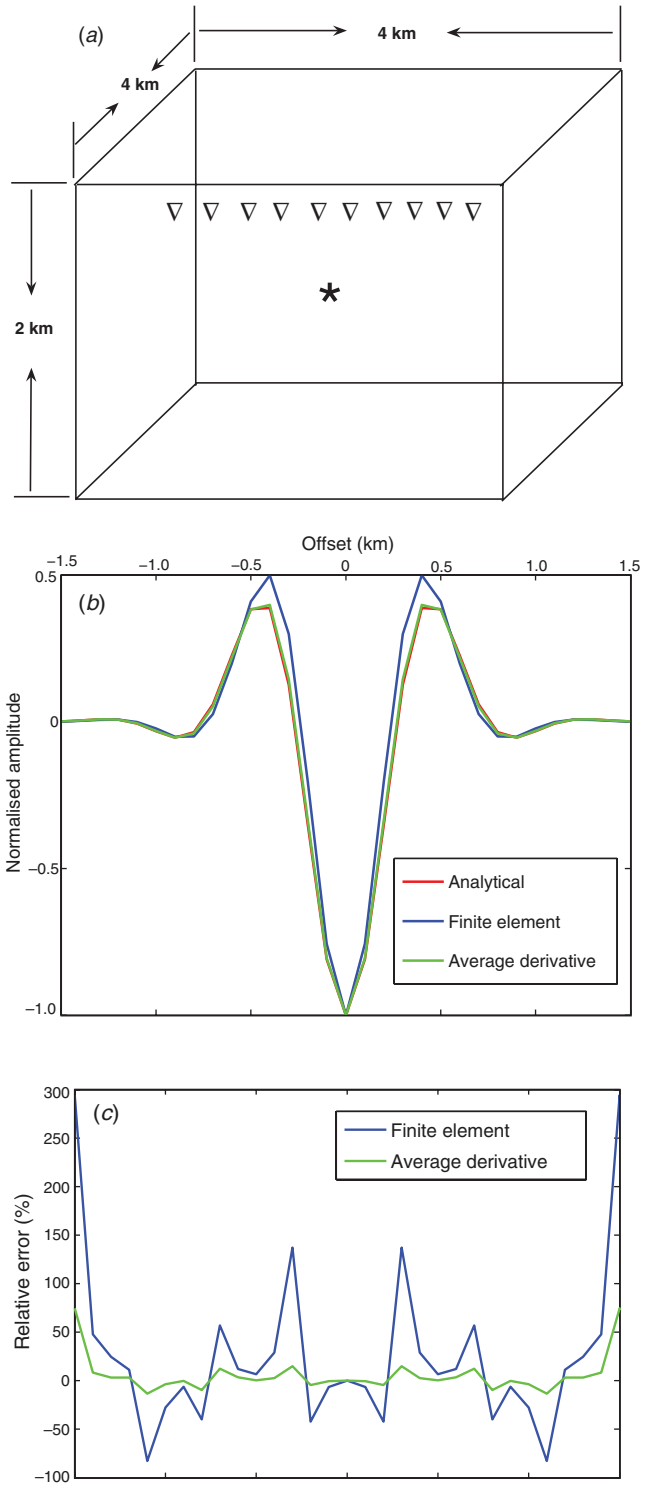

Fig. 10. (*a*) The homogeneous model. * represents the source. ∇ represents the receiver. (*b*) Laplace-Fourier-domain wavefields computed with the analytical method, the 27-point finite-element scheme, and the 27-point average-derivative optimal scheme. (*c*) The corresponding relative errors. The result for the average-derivative scheme is in good agreement with the analytical result, while the result for the finite-element scheme shows amplitude errors.

$x = 4$ km, $y = 4$ km, and $z = 2$ km, respectively. A temporal impulse is placed at the centre of the model as a source. The receivers are placed at a depth of 500 m. The angular frequency ω is taken to be 10π/s. The Laplace damping constant s is taken to be 5π/s. Horizontal sampling intervals are $\Delta x = \Delta y = 100$ m. Vertical sampling interval is taken as $\Delta z = \Delta x/2 = 50$ m. For this ratio of directional sampling intervals, the optimisation coefficients of the 27-point average-derivative optimal scheme (Equation 2) are $\alpha_1 = 0.083375$, $\alpha_2 = 0.000000$, $\beta_1 = 0.083357$, $\beta_2 = 0.000000$, $\gamma_1 = 0.083358$, $\gamma_2 = 0.000000$, $c = 0.499935$, $d = 0.083344$, and $e = 0.000000$ (Table 1).

In this example, analytical solution is available to make comparisons with numerical solutions:

$$P(x, y, z, \omega, s) = \frac{1}{r}\exp\left\{\frac{\omega - \mathrm{i}s}{v}r\right\}, \tag{13}$$

where

$$r = \sqrt{(x - x_0)^2 + (y - y_0)^2 + (z - z_0)^2},$$

where (x_0, y_0, z_0) is the source position.

In numerical comparisons, the following relative error of Laplace-domain wavefield is used

$$RE = \left|\frac{w_c - w_a}{w_a}\right|, \tag{14}$$

where w_c and w_a are the calculated wavefield and the analytical wavefield, respectively.

Figure 10*b* shows the normalised Laplace-Fourier-domain seismograms (real part) computed with the analytical formula (Equation 13), the 27-point finite-element scheme (Equation 3) and the 27-point average-derivative optimal scheme (Equation 2). Figure 10*c* shows the corresponding relative errors of the 27-point finite-element scheme (Equation 3) and the 27-point average-derivative optimal scheme (Equation 2). The result computed with the 27-point average-derivative optimal scheme (Equation 2) is in good agreement with the analytical result. For the result computed with the 27-point finite-element scheme (Equation 3), there are amplitude errors which become larger as the offset increases because the scheme's dispersion errors become larger as the propagation angle increases. The computational cost is the same for these two 27-point schemes, which indicates the superiority of the 27-point Laplace-Fourier-domain average-derivative optimal scheme to the 27-point Laplace-Fourier-domain finite-element scheme.

Discussion

By reducing the required number of grid points per wavelength and pseudo-wavelength by a factor of approximately three, the 27-point average-derivative optimal scheme can accommodate a sampling interval approximately three times larger in comparison with the 27-point finite-element scheme. Therefore, compared to the 27-point finite-element scheme, the 27-point average-derivative optimal scheme can achieve computational efficiency improvement by at least a factor of 27. This is very important for modelling and FWI based on the 3D Laplace-Fourier-domain scalar wave equation. However, the 27-point average-derivative optimal scheme still requires seven grid points per wavelength and pseudo-wavelength. More accurate schemes should be further developed. The purpose of this paper is just to provide such a theoretical framework for Laplace-Fourier-domain dispersion analysis to develop schemes of high accuracy. I only considered a homogeneous medium to confirm the results of dispersion analysis. Numerical experiments with more complex media and possible applications to real data remain to be done. But these aspects are beyond the scope of this paper.

Conclusions

A method for performing numerical dispersion analysis for 3D Laplace-Fourier-domain scalar wave equation has been

developed. Based on this method and the optimisation technique, a 27-point average-derivative optimal scheme has been derived. Compared to the 27-point finite-element scheme, the 27-point average-derivative optimal scheme reduces the number of grid points per wavelength and pseudo-wavelength from 23 to 7 for both equal and unequal directional sampling intervals. Comparisons with the analytical solution for a homogenous model demonstrate that the 27-point Laplace-Fourier-domain average-derivative is superior to the 27-point Laplace-Fourier-domain finite-element scheme.

Acknowledgements

I would like to thank the anonymous reviewers for valuable suggestions. This work is supported by the National Natural Science Foundation of China under grant numbers 41474104 and 41274139.

References

Brenders, A. J., and Pratt, R. G., 2007, Full waveform tomography for lithospheric imaging: results from a blind test in a realistic crustal model: *Geophysical Journal International*, **168**, 133–151.

Bunks, C., Salek, F. M., Zaleski, S., and Chavent, G., 1995, Multiscale seismic waveform inversion: *Geophysics*, **60**, 1457–1473.

Chen, J.-B., 2014*a*, Laplace-Fourier-domain dispersion analysis of an average derivative optimal scheme for scalar wave equation: *Geophysical Journal International*, **197**, 1681–1692.

Chen, J.-B., 2014*b*, A 27-point scheme for a 3D frequency-domain scalar wave equation based on an average-derivative method: *Geophysical Prospecting*, **62**, 258–277.

Pyun, S., Son, W., and Shin, C., 2011, 3D acoustic waveform inversion in the Laplace domain using an iterative solver: *Geophysical Prospecting*, **59**, 386–399.

Shin, C., and Cha, Y. H., 2009, Waveform inversion in the Laplace-Fourier domain: *Geophysical Journal International*, **177**, 1067–1079.

Um, E. S., Commer, M., and Newman, G. A., 2012, Iterative finite-difference solution analysis of acoustic wave equation in the Laplace-Fourier domain: *Geophysics*, **77**, T29–T36.

Virieux, J., and Operto, S., 2009, An overview of full-waveform inversion in exploration geophysics: *Geophysics*, **74**, WCC1–WCC26.